

# Sub-ångström cryo-EM structure of a prion protofibril reveals a polar clasp

Marcus Gallagher-Jones<sup>1</sup>, Calina Glynn<sup>1</sup>, David R. Boyer<sup>2</sup>, Michael W. Martynowycz<sup>3</sup>, Evelyn Hernandez<sup>1</sup>, Jennifer Miao<sup>1</sup>, Chih-Te Zee<sup>1</sup>, Irina V. Novikova<sup>4</sup>, Lukasz Goldschmidt<sup>2</sup>, Heather T. McFarlane<sup>2</sup>, Gustavo F. Helguera<sup>5</sup>, James E. Evans<sup>4</sup>, Michael R. Sawaya<sup>2</sup>, Duilio Cascio<sup>2</sup>, David S. Eisenberg<sup>1,2</sup>, Tamir Gonen<sup>3</sup> and Jose A. Rodriguez<sup>1\*</sup>

**The atomic structure of the infectious, protease-resistant,  $\beta$ -sheet-rich and fibrillar mammalian prion remains unknown. Through the cryo-EM method MicroED, we reveal the sub-ångström-resolution structure of a protofibril formed by a wild-type segment from the  $\beta 2$ - $\alpha 2$  loop of the bank vole prion protein. The structure of this protofibril reveals a stabilizing network of hydrogen bonds that link polar zippers within a sheet, producing motifs we have named 'polar clasps'.**

Micro electron diffraction (MicroED) is a cryo-EM method that facilitates the determination of atomic structures from sub-micrometer-thin protein nanocrystals and fragmented crystallites<sup>1–3</sup>. Several high-resolution amyloid structures have been determined by MicroED, including two structures from the toxic core of the Parkinson's-associated protein  $\alpha$ -synuclein<sup>4</sup>, two from the type-2-diabetes-associated protein IAPP<sup>5</sup>, and five ab initio structures<sup>2,6</sup>. These structures add to those of the fibril cores of  $\alpha$ -synuclein<sup>7</sup>, amyloid- $\beta$  (ref. <sup>8</sup>), tau<sup>9</sup>, and a fungal prion<sup>10</sup> recently determined by complementary methods. However, an atomic structure of the infectious scrapie form of the mammalian prion protein (PrP<sup>Sc</sup>) remains unknown<sup>11</sup>. PrP<sup>Sc</sup> shares some structural hallmarks of amyloid, appearing as rope-like filaments or rods made of tightly mating  $\beta$ -sheets<sup>12,13</sup>. However, PrP<sup>Sc</sup> also differs from other amyloids: it resists proteolysis and denaturation, is infectious, and can spread within and between species to cause disease<sup>11,14,15</sup>.

To evaluate the source of PrP<sup>Sc</sup> stability, we investigated segments in mammalian prion proteins (PrP) that might form the core of PrP<sup>Sc</sup> fibrils. Informed by structure-based prediction of amyloid-prone sequences<sup>16</sup>, we identified 168-QYNNQNNFV-176, a segment of the  $\beta 2$ - $\alpha 2$  loop of the bank vole (*Myodes glareolus*) PrP (Fig. 1), a universal prion acceptor<sup>17,18</sup>. This segment lies within the predicted cross- $\beta$  core of PrP fibrils (Supplementary Fig. 1), shows high conservation in rodents and other mammals (Supplementary Fig. 1), and is rich in asparagines<sup>19,20</sup>, which may stabilize prion fibrils<sup>21</sup>. At sub-millimolar concentrations, this segment produces highly ordered aggregates (Supplementary Fig. 2) that, when aligned and illuminated by X-rays, produce cross- $\beta$  diffraction (Supplementary Fig. 2). Like PrP<sup>Sc</sup>, aggregates formed by this segment are resistant to high concentrations of urea, guanidine, and a range of pH, but are sensitive to sodium hydroxide (Supplementary Fig. 3). Given its shared biophysical

properties with PrP<sup>Sc</sup>, we labeled our segment proto-PrP<sup>Sc</sup> and set out to uncover the structural basis for its stability.

From optimized microcrystals (Supplementary Fig. 4), we determined a microfocus X-ray diffraction structure of proto-PrP<sup>Sc</sup> to 1.1-Å resolution by molecular replacement (Supplementary Fig. 4 and Supplementary Table 1). The conditions in which we observed microcrystals of proto-PrP<sup>Sc</sup> also produced showers of nanocrystals, evident in electron micrographs (Fig. 1). These nanocrystals diffracted to 0.72 Å by MicroED (Fig. 1). Merging diffraction from multiple crystals, we achieved a high-completeness 0.75-Å-resolution dataset (Supplementary Table 1). From these data, we obtained an ab initio solution that was similar to our microfocal X-ray diffraction structure of proto-PrP<sup>Sc</sup> (Supplementary Fig. 4) and suitable for atomic refinement (Supplementary Fig. 5). This ultrahigh-resolution MicroED structure of proto-PrP<sup>Sc</sup> shows features that are invisible in the X-ray structure and critical to our understanding of its stability.

The structure of proto-PrP<sup>Sc</sup> reveals a prion protofibril with amyloid-like features:  $\beta$ -strands parallel and in register as a class 2 steric zipper<sup>12</sup> in which sheets pair front to back (Fig. 2). Two tightly mating curved sheets make up the proto-PrP<sup>Sc</sup> fibril (Fig. 2), although side chains in these sheets interdigitate less in proto-PrP<sup>Sc</sup> than those observed in conventional amyloid structures<sup>12</sup>. Although sheets stack in a parallel face-to-back configuration, the convex face of one sheet nestles against the concave face of its neighbor, approximately 10.3 Å away, with a high degree of surface complementarity ( $S_s$ , 0.807) (Fig. 2). The interface between these sheets is large, concealing 204.5 Å<sup>2</sup> per strand, and is entirely devoid of waters at its core (Fig. 1). Atoms in the MicroED structure of proto-PrP<sup>Sc</sup> are extremely well ordered, with an average  $B$  factor of 6.0 Å<sup>2</sup> overall and 2.8 Å<sup>2</sup> within its core (Supplementary Fig. 6 and Supplementary Table 1). These values are less than half of the overall  $B$  factor in our X-ray diffraction structure of proto-PrP<sup>Sc</sup> (Supplementary Table 1), thus confirming a greater degree of order in our nanocrystallites compared to that of larger microcrystals of the same segment.

A 3D network of hydrogen bonds stabilizes proto-PrP<sup>Sc</sup> (Supplementary Table 2); hydrogens at its core participate in intra-residue C5 bonds<sup>22</sup> (Fig. 3), and asparagine and glutamine residues stack along its fibril axis (Fig. 2). Glutamines and asparagines

<sup>1</sup>Department of Chemistry and Biochemistry, UCLA-DOE Institute for Genomics and Proteomics, University of California Los Angeles, Los Angeles, CA, USA. <sup>2</sup>Department of Biological Chemistry and Department of Chemistry and Biochemistry, University of California Los Angeles, Howard Hughes Medical Institute, UCLA-DOE Institute for Genomics and Proteomics, Los Angeles, CA, USA. <sup>3</sup>Janelia Research Campus, Howard Hughes Medical Institute, Ashburn, VA, USA. <sup>4</sup>Environmental Molecular Sciences Laboratory, Pacific Northwest National Laboratory, Richland, WA, USA. <sup>5</sup>Laboratory of Pharmaceutical Biotechnology, Institute of Biology and Experimental Medicine, Buenos Aires, Argentina. Marcus Gallagher-Jones and Calina Glynn contributed equally to this work. \*e-mail: [jrodriguez@mbi.ucla.edu](mailto:jrodriguez@mbi.ucla.edu)

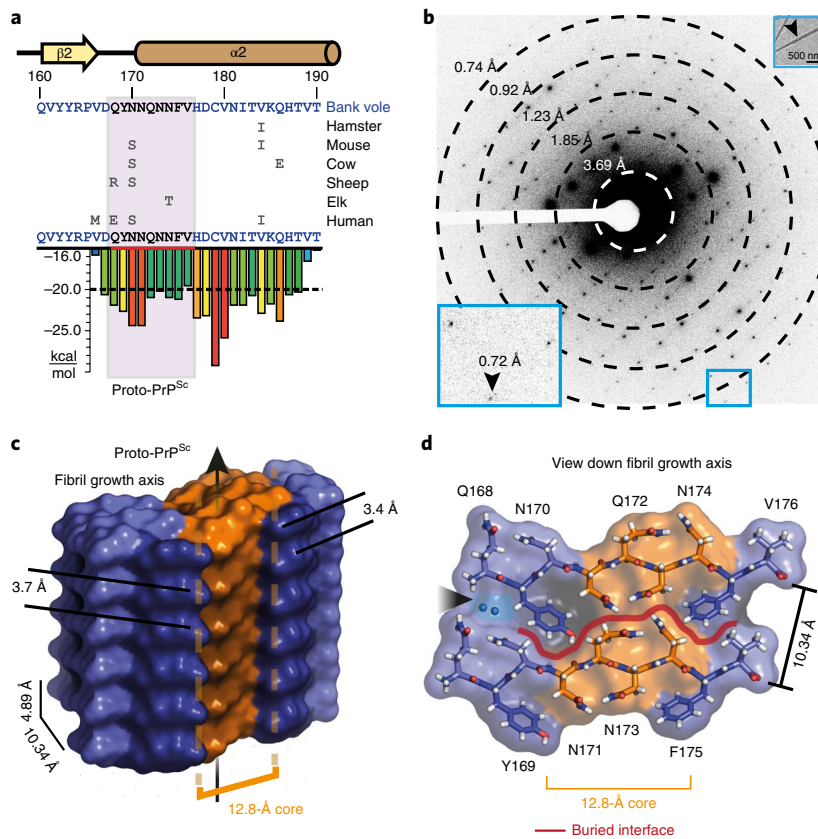


**Fig. 1 | Structure of proto-PrP<sup>Sc</sup> from sub-ångström diffraction of nanoscale crystals by MicroED.** **a**, Sequence of the bank vole PrP  $\beta$ 2- $\alpha$ 2 loop, highlighting local secondary structure and variation in sequence compared to hamster, mouse, cow, sheep, elk, and human. The sequence of proto-PrP<sup>Sc</sup> is highlighted in a plot that indicates propensity for amyloid formation (scored in kcal/mol). The region encoding proto-PrP<sup>Sc</sup> is boxed in magenta. **b**, Single MicroED image showing strong diffraction to 0.72 Å (inset). A second inset shows a proto-PrP<sup>Sc</sup> crystal probed by MicroED (arrow). **c,d**, Side (**c**) and top (**d**) views of the proto-PrP<sup>Sc</sup>-molecular surface. Stacked aromatics are colored dark purple, a conformationally constrained core region is colored orange, two waters are noted with a black arrow, and a red line indicates the interface between sheets in **d**.

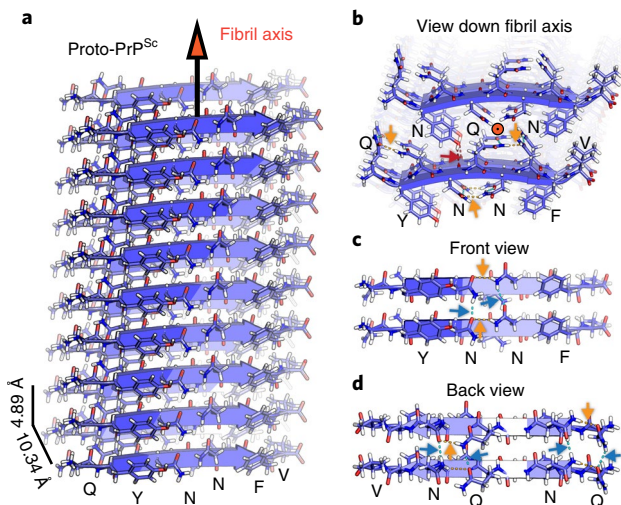


**Fig. 2 | Filament structure of proto-PrP<sup>Sc</sup> and its stabilizing network of hydrogen bonds.** **a**, Structure of proto-PrP<sup>Sc</sup> determined by MicroED shown as an assembly of eighteen strands. Distances between strands and sheets and the fibril growth axis are labeled. **b**, A view down the fibril axis highlighting the interface between adjacent sheets. An orange circle denotes the direction of the fibril axis. **c,d**, Front (**c**) and back (**d**) views of two strands of a sheet. Polar contacts are labeled as orange arrows for intrachain and blue arrows for interchain. A single intersheet hydrogen bond is labeled by a red arrow.

in proto-PrP<sup>Sc</sup> form networks of hydrogen bonds reminiscent of proton wires<sup>23</sup>, polar ladders<sup>24</sup>, and the polar zippers first proposed by Max Perutz<sup>25,26</sup> (Supplementary Fig. 7). Neighboring polar ladders in proto-PrP<sup>Sc</sup> are additionally linked by hydrogen bonds within a strand (Fig. 3), a motif we refer to as a 'polar clasp' (Supplementary Fig. 7). Stacks of phenylalanine and tyrosine residues shield clasps at the core of proto-PrP<sup>Sc</sup> (Figs. 1 and 2). The importance of this aromatic embrace is underscored by a lack of clasps in structures of shorter segments from this region of PrP that lack Tyr169 (refs. 12,27). On this evidence, we hypothesize that polar clasps and stacked aromatic residues act in concert to stabilize proto-PrP<sup>Sc</sup>, as they might for PrP<sup>Sc</sup>.

Our hypothesis of proto-PrP<sup>Sc</sup> stability relies on the locations of hydrogen atoms throughout the structure. Hydrogens in the MicroED structure of proto-PrP<sup>Sc</sup> are unambiguously assigned, informed by pronounced difference density in ultrahigh-resolution maps (Supplementary Figs. 5, 8, and 9 and Supplementary Table 4). Hydrogens at the core of proto-PrP<sup>Sc</sup> are as evident as those seen in structures of small organic compounds determined by electron diffraction<sup>28</sup>, including our own structure of carbamazepine (Supplementary Fig. 10 and Supplementary Table 3). Density in ultrahigh-resolution maps of proto-PrP<sup>Sc</sup> suggests that hydrogen may occupy positions that deviate from idealized geometry (Supplementary Fig. 5). Improved hydrogen positions indicated by ultrahigh-resolution maps in MicroED could bolster the accuracy of calculations based on observed hydrogen bond networks.

Ultrahigh-resolution maps of proto-PrP<sup>Sc</sup> mirror features that appear in electron density maps of the highest resolution X-ray

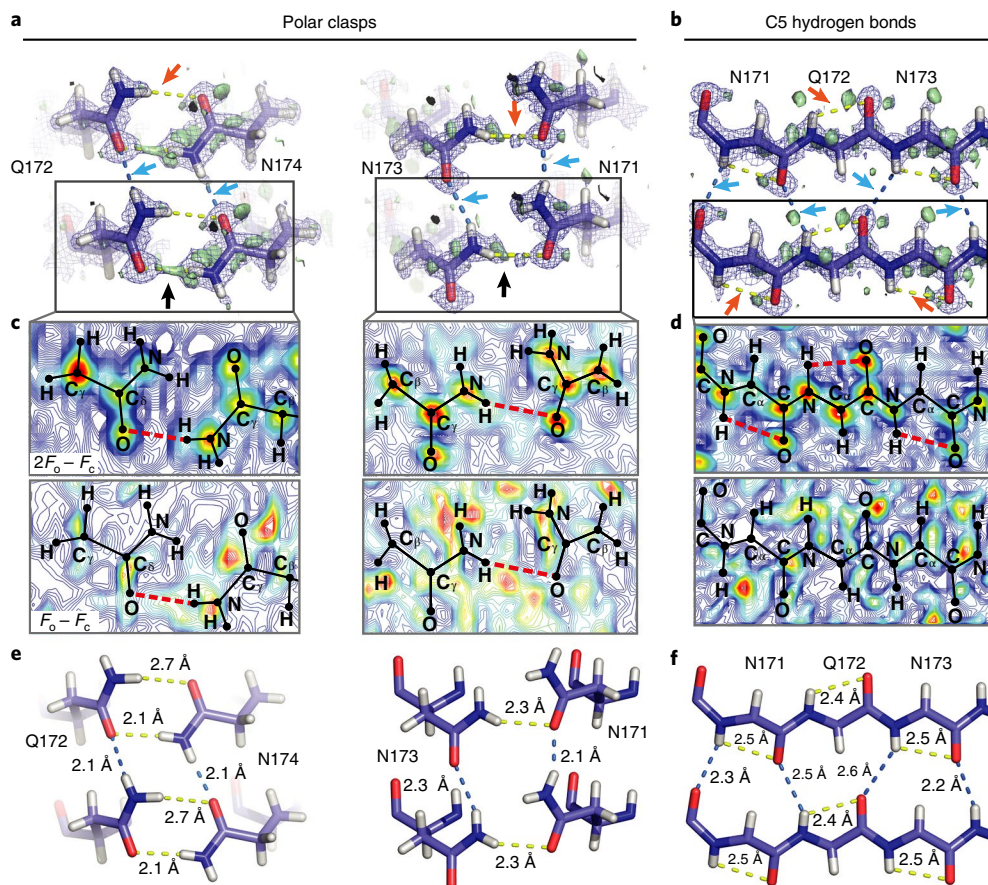


**Fig. 3 | Sub-ångström cryo-EM maps show stabilizing hydrogen bonds in proto-PrP<sup>Sc</sup>.** **a**, Polar clasps formed by hydrogen bonds that link Q172 to N174 and N171 to N173. **b**, C5 hydrogen bonds (orange arrows) in the context of backbone hydrogen bonds (blue arrows) at the core of proto-PrP<sup>Sc</sup>. Bridging density can be seen in both the  $2F_o - F_c$  and  $F_o - F_c$  maps (purple mesh and green isosurface, respectively) for a subset of the hydrogen bonds (black arrows). **c,d**, Contour maps show  $2F_o - F_c$  or  $F_o - F_c$  density for polar clasps (**c**) and C5 bonds (**d**). Contours are averaged over a  $\sim 1.5$ -Å-thick volume with high contour values shown in red, low values in blue, and hydrogen bonds as dashed red lines. **e,f**, Distances for both intrachain (yellow lines) and interchain (blue lines) hydrogen bonds are highlighted in polar clasps (**e**) and C5 bonds (**f**).

structures and show similar residual density, which in the latter is assigned to valence electrons<sup>29</sup> (Supplementary Fig. 9). In addition, in polar clasps at the core of proto-PrP<sup>Sc</sup>, density is seen surrounding donor hydrogens and oxygen acceptors (Fig. 3 and Supplementary Figs. 5 and 9). This density is not explicitly accounted for by our atomic model during refinement and is not evident in maps of other small molecules determined by MicroED or in lower-resolution maps of proto-PrP<sup>Sc</sup> (Supplementary Figs. 8 and 10 and Supplementary Table 4). However, this density is preserved across maps produced by refinement programs with different scattering factor libraries (Supplementary Fig. 11). A full account of the complex features present in ultrahigh-resolution cryo-EM maps may require advances in refinement that incorporate molecular vibrations, crystal bending, non-kinematic scattering and chemical bonding<sup>29–33</sup>.

Through MicroED, cryo-EM surpasses the 1-Å barrier and yields the structure of proto-PrP<sup>Sc</sup>, a denaturant-resistant prion protofibril. Cryo-EM maps of proto-PrP<sup>Sc</sup> at 0.75-Å resolution reveal a 3D network of stabilizing hydrogen bonds that link residues between and within its  $\beta$ -strands through polar clasps.

## Methods

Methods, including statements of data availability and any associated accession codes and references, are available at <https://doi.org/10.1038/s41594-017-0018-0>.

Received: 9 November 2017; Accepted: 7 December 2017;  
Published online: 15 January 2018

## References

- Shi, D., Nannenga, B. L., Iadanza, M. G. & Gonen, T. Three-dimensional electron crystallography of protein microcrystals. *eLife* **2**, e01345 (2013).
- de la Cruz, M. J. et al. Atomic-resolution structures from fragmented protein crystals with the cryoEM method MicroED. *Nat. Methods* **14**, 399–402 (2017).
- Rodriguez, J. A., Eisenberg, D. S. & Gonen, T. Taking the measure of MicroED. *Curr. Opin. Struct. Biol.* **46**, 79–86 (2017).
- Rodriguez, J. A. et al. Structure of the toxic core of  $\alpha$ -synuclein from invisible crystals. *Nature* **525**, 486–490 (2015).
- Krotoe, P. et al. Atomic structures of fibrillar segments of hIAPP suggest tightly mated  $\beta$ -sheets are important for cytotoxicity. *eLife* **6**, e19273 (2017).
- Sawaya, M. R. et al. Ab initio structure determination from prion nanocrystals at atomic resolution by MicroED. *Proc. Natl. Acad. Sci. USA* **113**, 11232–11236 (2016).
- Tuttle, M. D. et al. Solid-state NMR structure of a pathogenic fibril of full-length human  $\alpha$ -synuclein. *Nat. Struct. Mol. Biol.* **23**, 409–415 (2016).
- Schmidt, M. et al. Peptide dimer structure in an  $A\beta(1-42)$  fibril visualized with cryo-EM. *Proc. Natl. Acad. Sci. USA* **112**, 11858–11863 (2015).
- Fitzpatrick, A. W. P. et al. Cryo-EM structures of tau filaments from Alzheimer's disease. *Nature* **547**, 185–190 (2017).
- Wasmer, C. et al. Amyloid fibrils of the HET-s(218–289) prion form a  $\beta$  solenoid with a triangular hydrophobic core. *Science* **319**, 1523–1526 (2008).
- Rodriguez, J. A., Jiang, L. & Eisenberg, D. S. Toward the atomic structure of PrP<sup>Sc</sup>. *Cold Spring Harb. Perspect. Biol.* **9**, a031336 (2017).

12. Sawaya, M. R. et al. Atomic structures of amyloid cross-beta spines reveal varied steric zippers. *Nature* **447**, 453–457 (2007).
13. Eisenberg, D. & Jucker, M. The amyloid state of proteins in human diseases. *Cell* **148**, 1188–1203 (2012).
14. McKinley, M. P., Bolton, D. C. & Prusiner, S. B. A protease-resistant protein is a structural component of the scrapie prion. *Cell* **35**, 57–62 (1983).
15. Kurt, T. D. & Sigurdson, C. J. Cross-species transmission of CWD prions. *Prion* **10**, 83–91 (2016).
16. Goldschmidt, L., Teng, P. K., Riek, R. & Eisenberg, D. Identifying the amyloids, proteins capable of forming amyloid-like fibrils. *Proc. Natl. Acad. Sci. USA* **107**, 3487–3492 (2010).
17. Watts, J. C. et al. Evidence that bank vole PrP is a universal acceptor for prions. *PLoS Pathog.* **10**, e1003990 (2014).
18. Kurt, T. et al. The molecular basis for cross-species prion transmission. *FASEB J.* **30**, 814.7 (2016).
19. Halfmann, R. et al. Opposing effects of glutamine and asparagine govern prion formation by intrinsically disordered proteins. *Mol. Cell.* **43**, 72–84 (2011).
20. Zambrano, R. et al. PrionW: a server to identify proteins containing glutamine/asparagine rich prion-like domains and their amyloid cores. *Nucleic Acids Res.* **43**, W331–W337 (2015).
21. Kurt, T. D. et al. Asparagine and glutamine ladders promote cross-species prion conversion. *J. Biol. Chem.* <https://doi.org/10.1074/jbc.M117.794107> (2017).
22. Newberry, R. W. & Raines, R. T. A prevalent intrasid residue hydrogen bond stabilizes proteins. *Nat. Chem. Biol.* **12**, 1084–1088 (2016).
23. Nagle, J. F. & Morowitz, H. J. Molecular mechanisms for proton transport in membranes. *Proc. Natl. Acad. Sci. USA* **75**, 298–302 (1978).
24. Yoder, M. D., Lietzke, S. E. & Jurnak, F. Unusual structural features in the parallel  $\beta$ -helix in pectate lyases. *Structure* **1**, 241–251 (1993).
25. Perutz, M. F., Staden, R., Moens, L. & De Baere, I. Polar zippers. *Curr. Biol.* **3**, 249–253 (1993).
26. Perutz, M. F., Johnson, T., Suzuki, M. & Finch, J. T. Glutamine repeats as polar zippers: their possible role in inherited neurodegenerative diseases. *Proc. Natl. Acad. Sci. USA* **91**, 5355–5358 (1994).
27. Wiltzius, J. J. W. et al. Molecular mechanisms for protein-encoded inheritance. *Nat. Struct. Mol. Biol.* **16**, 973–978 (2009).
28. Palatinus, L. et al. Hydrogen positions in single nanocrystals revealed by electron diffraction. *Science* **355**, 166–169 (2017).
29. Hirano, Y., Takeda, K. & Miki, K. Charge-density analysis of an iron-sulfur protein at an ultra-high resolution of 0.48 Å. *Nature* **534**, 281–284 (2016).
30. Glaeser, R. M. & Downing, K. H. High-resolution electron crystallography of protein molecules. *Ultramicroscopy* **52**, 478–486 (1993).
31. Zhong, S., Dadarlat, V. M., Glaeser, R. M., Head-Gordon, T. & Downing, K. H. Modeling chemical bonding effects for protein electron crystallography: the transferable fragmental electrostatic potential (TFESP) method. *Acta Crystallogr. A* **58**, 162–170 (2002).
32. Jelsch, C. et al. Accurate protein crystallography at ultra-high resolution: valence electron distribution in crambin. *Proc. Natl. Acad. Sci. USA* **97**, 3171–3176 (2000).
33. Zuo, J. M., Kim, M., O’Keeffe, M. & Spence, J. C. H. Direct observation of *d*-orbital holes and Cu–Cu bonding in Cu<sub>2</sub>O. *Nature* **401**, 49–52 (1999).

### Acknowledgements

We thank C. Ophus (Molecular Foundry-NCEM), J. Miao (UCLA), and H. Nelson (UCLA) for helpful discussions. This work is supported by DOE Grant DE-FC02-02ER63421, the EICN in the CNSI at UCLA, the Janelia Research Visitor Program, and the NE-CAT beamline 24-ID-E, funded by NIH-NIGMS P41 GM103403. This work was also supported by STROBE: a National Science Foundation Science and Technology Center under Grant No. DMR 1548924. G.F.H. is supported by the BEC.AR program, Fundación Bunge y Born, Fundación Williams, and Fundación René Barón, and is a member of CONICET. M.G.J. is supported by a QCB Collaboratory Postdoctoral Fellowship. C.G. is supported by the Cellular and Molecular Biology Training Program. J.A.R. is supported by the Searle Scholar Program and the Beckman Young Investigator Program. T.G. and D.S.E. are supported by the Howard Hughes Medical Institute (HHMI), and J.E.E. and I.V.N. are supported by the DOE-BER Molecules to Mesoscale Bioimaging Project FWP #66382.

### Author contributions

J.A.R. directed the work. J.A.R., J.M., E.H., M.W.M., and C.G. grew, evaluated, and optimized crystals. J.A.R., D.R.B., C.G., M.R.S., H.T.M., M.G.-J., C.-T.Z., I.V.N., J.E.E., and D.C. collected data. J.A.R., C.G., J.M., M.G.-J., M.R.S., D.C., M.W.M., G.F.H., E.H., L.G., D.S.E., and T.G. analyzed the data. C.G., M.G.-J., and J.A.R. wrote the article, with input from all authors.

### Competing interests

The authors declare no competing interests.

### Additional information

**Supplementary information** is available for this paper at <https://doi.org/10.1038/s41594-017-0018-0>.

**Reprints and permissions information** is available at [www.nature.com/reprints](http://www.nature.com/reprints).

**Correspondence and requests for materials** should be addressed to J.A.R.

**Publisher’s note:** Springer Nature remains neutral with regard to jurisdictional claims in published maps and institutional affiliations.

## Methods

**Phylogenetic and sequence analysis of bank vole PrP 27–30.** The top 130 most similar wild-type sequences to bank vole PrP 90–231 were generated using NCBI BLAST. Of these 130 sequences, all sequences containing the proto-PrP<sup>Sc</sup> peptide were selected and aligned.

**Characterization of proto-PrP<sup>Sc</sup> peptide.** The synthetic peptide, QYNNQNFV, corresponding to residues 168–176 of the bank vole prion protein was purchased from GenScript. The peptide used for our experiments was received at >98% purity achieved by reverse-phase HPLC. The peptide was qualified on a Bruker (ultrafleXtreme) MALDI-TOF/TOF mass spectrometer, reported as *m/z* (intensity, arbitrary units). The spectrum has a mass list that includes a [M+H]<sup>+</sup> peak at 1,141.3 Da (expected 1,140.5 Da), a [M+Na]<sup>+</sup> peak at 1,163.4 Da (expected 1,162.49 Da), and a [M+K]<sup>+</sup> peak at 1,179.3 Da (1,178.46 Da).

**Characterization of carbamazepine.** Lyophilized powder of carbamazepine (5H-dibenzo[b,f]azepine-5-carboxamide, C<sub>15</sub>H<sub>12</sub>N<sub>2</sub>O) with purity >99% was purchased from Sigma-Aldrich and crystallized without further purification.

**Aggregation of proto-PrP<sup>Sc</sup>.** Proto-PrP<sup>Sc</sup> peptide was solubilized in ultrapure water at 0.22–1.75 mM. 50 μL of each sample was added to a 96-well clear flat-bottom plate in triplicate and evaluated for aggregate formation by reading absorbance at 350 nm on an Infinite M1000 Pro plate reader (Tecan). Readings were measured immediately after solubilization after 3 h and after 6 h of shaking at 900 r.p.m. at 37 °C. Wells were imaged after 6 h using a Leica M205 C light microscope (Leica Microsystems) and after 3 and 6 h by electron microscopy as described below. Electron microscope images are representative of more than five images taken at each concentration and time point.

**Fibril diffraction from proto-PrP<sup>Sc</sup> aggregates.** Solutions containing aggregates of proto-PrP<sup>Sc</sup> were clarified by centrifugation. Pelleted aggregates were resuspended in a concentrated volume in water, applied between two pulled capillaries and left to dry overnight. Oriented aggregates formed between the capillary ends were resupplied with additional solution containing aggregates and left to dry again. This process was repeated several times to grow the bulk of aligned aggregates on a capillary. Aligned aggregates were then diffracted using 5-min exposures to a FRE+ rotating anode generator with VARIMAX HR confocal optics producing Cu K-α radiation (Rigaku, Tokyo, Japan) and detected using a RIGAKU R-AXIS HTC imaging plate detector at a distance of 156 mm from the source.

**Chemical denaturation of proto-PrP<sup>Sc</sup> aggregates.** Proto-PrP<sup>Sc</sup> was solubilized at approximately 3.5 mM and allowed to form aggregates. This solution was diluted to approximately 1:4 before treatment with either 0.5–6.0 M urea, 0.5–4.5 M guanidinium-HCl, 0.75 M HCl, 0.75 M of either MES, pH 2, acetate, pH 4, MES, pH 6, Tris-HCl, pH 8 or 10, or 0.75 M NaOH. Aggregate content was measured by absorbance compared to a control solution consisting of 0.01% (w/v) 1-μm latex spheres in water. Spectra across the visible range (250–700 nm) were collected using a Nanodrop One (Thermo).

**Growth of proto-PrP<sup>Sc</sup> crystals.** Peptide powder was weighed and dissolved in ultrapure water at near maximum solubility, 3.5 mM. Crystals were grown at room temperature by the hanging-drop method in a 96-well Wizard screen. Crystals appeared in various conditions and were further optimized in 24-well hanging-drop vapor diffusion experiments. The best crystals of proto-PrP<sup>Sc</sup> grew within 24 h at a peptide concentration of 1.75 mM in the presence of 0.1 M 2-(*N*-morpholino) ethanesulfonic acid (MES), pH 6.0, and either 10% ethanol or 10% 2-Methyl-2,4-pentanediol (MPD).

**Transmission electron microscopy.** Approximately 2 μL of aggregated proto-PrP<sup>Sc</sup> were applied to 300-mesh Formvar-carbon coated grids (Ted Pella Inc.) for 2 min before excess liquid was removed and grids left to dry. Grids were imaged either on a Tecnai T12 or F20 electron microscope (Thermo Fisher, formerly FEI). Samples were imaged at a magnification of 2,100× with a dose rate of <30 e<sup>-</sup>/Å<sup>2</sup>.

**Microfocus X-ray data collection.** Crystals grown in 0.1 M MES, pH 6.0, and 10% ethanol and mixed with 100% glycerol as cryoprotectant were harvested from 24-well hanging drops using MiTeGen loops and flash frozen in liquid nitrogen. 73 diffraction images were collected, each spanning a 3° wedge, from a single crystal at a temperature of 100 K at the advanced photon source (APS) beamline 24-ID-E, equipped with an ADSC Q315 CCD detector, using a 10-μm beam with a 0.98-Å wavelength.

**Microfocus X-ray data processing and structure determination.** Diffraction images collected from a single crystal of proto-PrP<sup>Sc</sup> were indexed and integrated in Denzo, yielding a dataset with 80.75% overall completeness at 1.1-Å resolution in space group *P1*. A suitable molecular replacement solution was obtained from this data using the PHASER program and an idealized β-strand nonapeptide alanine model as a probe. The model was refined using REFMAC against the measured data to a final  $R_{\text{work}} / R_{\text{free}}$  of 0.14 / 0.16.

**MicroED sample preparation.** Nanoscale needle crystals of proto-PrP<sup>Sc</sup> were grown in batch in 0.1 M MES, pH 6.0, and 10% ethanol. Crystals were diluted in mother liquor and fragmented by force of pipetting to create an approximately monodisperse solution of crystals. Carbamazepine was crystallized in batches by dilution into neat isopropanol at 100 μg/mL. 2 μL of either solution were placed on a holey carbon grid (1/4, 2/2, 2/4, #300 copper; Ted Pella Inc.) before plunge freezing into liquid ethane and transferring into liquid nitrogen for storage. Grids were held by a liquid-nitrogen-cooled Gatan 626 cryo-holder for transfer into and manipulation within the electron microscope.

**MicroED data collection.** MicroED data collection from nine sub-micron-thick needle crystals, and a single sub-micron carbamazepine crystal was performed as previously described<sup>34</sup>. Briefly, crystals of either proto-PrP<sup>Sc</sup> or carbamazepine lying in a frozen-hydrated state on holey carbon grids were inspected visually in overfocused diffraction mode on either a cryo-cooled FEI Tecnai F20 microscope operated at 200 kV (Janelia Research Campus) or a Titan environmental TEM operated at 300 kV (Environmental Molecular Sciences Lab, PNNL). Diffraction patterns used for structure determination were collected on a TVIPS TemCam-F416 CMOS detector in rolling-shutter mode with 3-s exposures while proto-PrP<sup>Sc</sup> crystals were unidirectionally rotated at a constant rate of 0.27° s<sup>-1</sup> over angular wedges ranging from -55° to +72°. A single carbamazepine crystal was rotated at a speed of 0.2° s<sup>-1</sup> over an angular wedge ranging between -45° to +45° with 5-s exposures. Beam intensity was held constant, with an average dose rate of 0.003–0.005 e<sup>-</sup> Å<sup>-2</sup> sec<sup>-1</sup>, corresponding to a total dose of ~1–3 e<sup>-</sup> Å<sup>-2</sup> per dataset. We used a camera length of 520 mm, the equivalent of a sample-to-detector distance of 950 mm in a corresponding lensless system. All diffraction was performed using a circular selected area aperture of ~1 μm<sup>2</sup> in projection.

**MicroED data processing.** Diffraction movies were converted to the SMV file format using TVIPS tools as previously described<sup>35</sup>. Indexing and integration were performed in XDS<sup>36</sup>. Integrated diffraction intensities from partial datasets of nine different proto-PrP<sup>Sc</sup> crystals were sorted and merged in XSCALE<sup>36</sup>. Merged intensities were converted to amplitudes at various resolution cutoffs to produce separate 1.1-Å, 1.0-Å, 0.9-Å, 0.8-Å, and 0.75-Å datasets. Ab initio structure determination was performed on each of these datasets using SHELXD<sup>37</sup>. Phases obtained from the atomic assembly generated by direct methods were used to produce maps of sufficient quality for subsequent model building in Coot<sup>38</sup> and refinement in Phenix<sup>39</sup> using electron scattering form factors to produce a final structure in space group *P1* with a final  $R_{\text{work}} / R_{\text{free}}$  of 24 / 25. Refinement in REFMAC was carried out in parallel to a final  $R_{\text{work}} / R_{\text{free}}$  of 23 / 25. The structure refined in Phenix (PDB 6AXZ) was used in all subsequent analysis and is shown in figures. Ab initio structure determination for carbamazepine was performed in SHELXT<sup>37</sup> in which a solution was found in space group *P21<sub>m</sub>* with no errors in chemical assignment or atom positions for all carbon, nitrogen, and oxygen atoms. This solution was refined in SHELXL<sup>37</sup> using electron form factors to an *R* value of 21.8%. A structure with hydrogen positions refined to best match difference density in the map lowered the *R* value to 19.8%.

**Analysis of buried surface area ( $S_b$ ) and surface complementarity ( $S_c$ ) for proto-PrP<sup>Sc</sup>.** The structure of proto-PrP<sup>Sc</sup> was used to calculate both  $S_b$  and  $S_c$  from an assembly consisting of two sheets generated by translational symmetry, each consisting of ten stacked β-strands.  $S_b$  was computed as an average of the buried surface area per chain in our assembly, calculated as the difference between the sum of the solvent-accessible surface area of the two sheets and the solvent-accessible surface area of the entire complex, divided by the total number of strands in both sheets.  $S_c$  was calculated using the CCP4 suite for all points at the interface between the two aforementioned sheets.

**Comparison of X-ray and MicroED structures.** Sequence alignment and structural superposition of both an individual chain and an assembly of two sheets from X-ray and MicroED structures of proto-PrP<sup>Sc</sup> were performed in PyMOL<sup>40</sup>. This alignment produced an all-atom r.m.s.d. of 0.162 Å, on which structural similarity was assessed.

**Analysis of aromatic residues in proto-PrP<sup>Sc</sup>.** Distances were measured between stacked aromatic residues that flank the core of proto-PrP<sup>Sc</sup>. Aromatics stacked between strands along planes separated by 3.7 or 3.4 Å for Y169 or F175, respectively, in a parallel-displaced configuration<sup>41</sup>. We measured the intersheet hydrogen bond created by Y169 to the backbone carbonyl of N171 on an opposing strand. Both Y169 and F175 formed aromatic ladders that channel polar residues into a 12.8-Å-long region at the core.

**Analysis of hydrogen bond networks.** Informed by the locations of hydrogens, visible in our maps at a 0.7–2.5-σ range, we evaluated hydrogen bond networks determined by the program HBplus (v.3.06)<sup>42</sup> and by manual inspection using PyMOL. We measured asparagine ladders between residues N170, N171, N173, and N174 and the corresponding asparagine residues on the strands above and below. We also measured glutamine ladders between residues Q168 and Q172 and their corresponding residues on strands above and below. We analyzed distances

associated with intrastrand hydrogen bonds formed by three pairs of residues: Q168–N170, N171–N173 and Q172–N174. Polar contacts were also measured between Q168–N170, with a 3.1-Å donor–acceptor (D–A) distance and a 2.3-Å H–O distance, Q172–N174, with a 3.0-Å D–A distance and a 2.1-Å H–O distance and N171–N173, with a 3.1-Å D–A distance and a 2.3-Å H–O distance. In each case, the linked residues faced the same side of the  $\beta$ -strand and bridged residues at positions (N/Q)<sup>1</sup> and (N)<sup>1+2</sup> within the strand. While the HBplus program does not identify C5 hydrogen bonds in our structure, we measured these bonds in residues N171, Q172, and N173, on the basis of the criteria that carbonyl oxygens bond with intraresidue amide protons if their geometry permits, with H–O distances shorter than 2.5 Å (ref. 23).

**Amylome profiling.** A subset of the predicted amyloyme was analyzed<sup>16</sup>, consisting of six-residue segments found to score favorably when threaded onto a template based on the structure of the yeast prion NNQQNY. We chose all segments that scored two s.d. better than the mean score for all peptides ( $Z$  score > 2). This subset of six-residue segments represents 95,381 out of 7,900,599 total segments, or 1.2% of all possible segments of this size in the human proteome. For each segment, we searched for a (Y/F) X (N/Q) X (N/Q) X (Y/F) motif across the region of the protein to which the segment belonged; a ten-residue window including two residues upstream and downstream of a profiled segment. QYNNQNNFV satisfies these metrics.

**Calculation of contour maps.**  $2F_o - F_c$  and  $F_o - F_c$  density maps were calculated from the final refined MTZ file using the FFT tool in CCP4. Maps were converted to MRC format in Chimera and imported into MATLAB. Contour plots were calculated such that the number of contours spanned the minimum to the maximum values of the maps with intervals of one s.d. ( $\sigma$ ) between contour levels.

**Life Sciences Reporting Summary.** Further information on experimental design is available in the Life Sciences Reporting Summary.

**Data availability.** Atomic coordinates and structure factors for proto-PrP<sup>Sc</sup> have been deposited in the EMDB and wwPDB; the structure obtained using MicroED is under accession codes EMD-7017 and PDB 6AXZ; the X-ray crystallography structure is under accession code PDB 6BTK. The structure of carbamazepine using microED has been deposited in the EMDB with accession code EMD-7287. Source data for all figures and files is available from the authors upon reasonable request, please see author contributions for specific datasets.

## References

- Shi, D. et al. The collection of MicroED data for macromolecular crystallography. *Nat. Protoc.* **11**, 895–904 (2016).
- Hattne, J., Shi, D., de la Cruz, M. J., Reyes, F. E. & Gonen, T. Modeling truncated pixel values of faint reflections in MicroED images. *J. Appl. Crystallogr.* **49**, 1029–1034 (2016).
- Kabsch, W. XDS. *Acta Crystallogr. D. Biol. Crystallogr.* **66**, 125–132 (2010).
- Sheldrick, G. M. A short history of SHELX. *Acta Crystallogr. A* **64**, 112–122 (2008).
- Emsley, P., Lohkamp, B., Scott, W. G. & Cowtan, K. Features and development of Coot. *Acta Crystallogr. D. Biol. Crystallogr.* **66**, 486–501 (2010).
- Adams, P. D. et al. PHENIX: a comprehensive Python-based system for macromolecular structure solution. *Acta Crystallogr. D. Biol. Crystallogr.* **66**, 213–221 (2010).
- Delano, W.L. *The PyMOL Molecular Graphics System* (DeLano Scientific, 2002).
- McGaughey, G. B., Gagné, M. & Rappé, A. K.  $\pi$ -Stacking interactions. Alive and well in proteins. *J. Biol. Chem.* **273**, 15458–15463 (1998).
- McDonald, I. K. & Thornton, J. M. Satisfying hydrogen bonding potential in proteins. *J. Mol. Biol.* **238**, 777–793 (1994).

## Life Sciences Reporting Summary

Nature Research wishes to improve the reproducibility of the work that we publish. This form is intended for publication with all accepted life science papers and provides structure for consistency and transparency in reporting. Every life science submission will use this form; some list items might not apply to an individual manuscript, but all fields must be completed for clarity.

For further information on the points included in this form, see [Reporting Life Sciences Research](#). For further information on Nature Research policies, including our [data availability policy](#), see [Authors & Referees](#) and the [Editorial Policy Checklist](#).

### ► Experimental design

#### 1. Sample size

Describe how sample size was determined.

Crystals were diffracted based on availability.

#### 2. Data exclusions

Describe any data exclusions.

Diffraction data sets were merged based on completeness, overall signal, and isomorphism. Crystals that led to excessively high merging errors were excluded from the final merge data set.

#### 3. Replication

Describe whether the experimental findings were reliably reproduced.

Crystal growth was reproducible under the conditions outlined.

#### 4. Randomization

Describe how samples/organisms/participants were allocated into experimental groups.

N/A.

#### 5. Blinding

Describe whether the investigators were blinded to group allocation during data collection and/or analysis.

N/A.

Note: all studies involving animals and/or human research participants must disclose whether blinding and randomization were used.

#### 6. Statistical parameters

For all figures and tables that use statistical methods, confirm that the following items are present in relevant figure legends (or in the Methods section if additional space is needed).

n/a Confirmed

- The exact sample size ( $n$ ) for each experimental group/condition, given as a discrete number and unit of measurement (animals, litters, cultures, etc.)
- A description of how samples were collected, noting whether measurements were taken from distinct samples or whether the same sample was measured repeatedly
- A statement indicating how many times each experiment was replicated
- The statistical test(s) used and whether they are one- or two-sided (note: only common tests should be described solely by name; more complex techniques should be described in the Methods section)
- A description of any assumptions or corrections, such as an adjustment for multiple comparisons
- The test results (e.g.  $P$  values) given as exact values whenever possible and with confidence intervals noted
- A clear description of statistics including central tendency (e.g. median, mean) and variation (e.g. standard deviation, interquartile range)
- Clearly defined error bars

See the web collection on [statistics for biologists](#) for further resources and guidance.

## ► Software

Policy information about [availability of computer code](#)

### 7. Software

Describe the software used to analyze the data in this study.

Software used is part of the CCP4 crystallographic processing suite of programs.

For manuscripts utilizing custom algorithms or software that are central to the paper but not yet described in the published literature, software must be made available to editors and reviewers upon request. We strongly encourage code deposition in a community repository (e.g. GitHub). *Nature Methods* [guidance for providing algorithms and software for publication](#) provides further information on this topic.

## ► Materials and reagents

Policy information about [availability of materials](#)

### 8. Materials availability

Indicate whether there are restrictions on availability of unique materials or if these materials are only available for distribution by a for-profit company.

N/A.

### 9. Antibodies

Describe the antibodies used and how they were validated for use in the system under study (i.e. assay and species).

N/A.

### 10. Eukaryotic cell lines

a. State the source of each eukaryotic cell line used.

N/A.

b. Describe the method of cell line authentication used.

N/A.

c. Report whether the cell lines were tested for mycoplasma contamination.

N/A.

d. If any of the cell lines used are listed in the database of commonly misidentified cell lines maintained by [ICLAC](#), provide a scientific rationale for their use.

N/A.

## ► Animals and human research participants

Policy information about [studies involving animals](#); when reporting animal research, follow the [ARRIVE guidelines](#)

### 11. Description of research animals

Provide details on animals and/or animal-derived materials used in the study.

N/A.

Policy information about [studies involving human research participants](#)

### 12. Description of human research participants

Describe the covariate-relevant population characteristics of the human research participants.

N/A.